Understanding the Optical Degradation of 845 nm Micro-Transfer-Printed VCSILs for Photonic Integrated Circuits

Michele Zenari, *Student Member, IEEE*, Matteo Buffolo, Mirko Fornasier, *Member, IEEE*, Carlo De Santi, *Member, IEEE*, Jeroen Goyvaerts, Alexander Grabowski, *Member, IEEE*, Johan Gustavsson, Sulakshna Kumari, Andim Stassren, Roel Baets, *Life Fellow, IEEE*, Anders Larsson, *Fellow, IEEE*, Günther Roelkens, *Senior Member, IEEE*, Gaudenzio Meneghesso, *Fellow, IEEE*, Enrico Zanoni, *Life Fellow, IEEE*, and Matteo Meneghini

***Abstract*— For the first time we investigate the optical degradation of vertical-cavity silicon-integrated lasers VCSILs) designed for operation at 845 nm in photonic integrated circuits (PICs). The study is based on the combined electro-optical characterization of VCSIL, submitted to constant-current stress tests at different current levels. The original results obtained within the manuscript indicate that degradation is related to the diffusion of impurities. Remarkably, depending on the region through which these impurities are migrating, the diffusion process affects device characteristics in different ways. During Phase 1 (Ph1), compensating impurities originating from the metal-semiconductor contact cross the top DBR, thus degrading mirror reflectivity, which is rarely observed in the literature, and leading to an increase in the threshold current of the device. As the impurities start reaching the active region we observe the onset of Phase 2 (Ph2), during which both threshold current and sub-threshold slope worsen, due to the increase of the Shockley-Read-Hall recombination rate. This phase is also characterized by a measurable increase in series resistance, which is ascribed to a change in the resistance of the oxide aperture. The identification of the root cause of physical degradation represents a fundamental step for future lifetime improvement of these novel optical sources, which are set to replace conventional solid-state sources in the 0.85 μm communication window.**

***Index Terms*— Degradation, VCSIL, diffusion, PICs.**

I. Introduction

PHOTONIC integrated circuits (PICs) allow for the integration of different optical functions on a single chip, allowing the realization of compact, cheap and robust optical systems. Photonic integrated circuits are currently predominantly being used for high-speed optical communication [1], [2]. Furthermore, PICs are also being adopted for developing biosensors [3], [4].

In both communication and sensing applications, one of the most critical components is the light source, typically a laser diode. Commonly, the lasers integrated into PIC platforms include edge-emitting lasers (EELs) such as distributed feedback (DFB) lasers and external cavity lasers. Promising optical sources for PICs operating in the 800 – 950 nm range are vertical-cavity surface-emitting lasers (VCSELs) [5]. VCSELs have different advantages compared to the aforementioned in-plane lasers: easier wafer-level testing, sub-mA threshold currents and high wall-plug efficiency and are currently widely deployed in short-range datacom applications, such as intra-data center data transmission [6].

The leading issue concerning the monolithic integration of III-V emitters (such as lasers) on silicon photonics platforms, which are widely used in modern PICs, is the lattice mismatch between the direct bandgap III-V active material and silicon. If heteroepitaxial integration is adopted, the lattice mismatch leads to the formation of highly defective semiconductor layers, and ultimately to poor device performance and lifetime [7]. A different approach is the micro-transfer-printing technique [8]. Commonly, lasers directly grown on silicon have lifetimes hovering around hundreds and thousands of hours [9], however, by leveraging the hybrid integration techniques (as micro-transfer printing), lifetimes of 100'000 hours

Manuscript received 9 November 2022; revised 8 March 2023 and 3 May 2023; accepted 1 June 2023. Date of publication 7 June 2023; date of current version 19 June 2023. This work was supported in part by the Italian Ministry of Education, Universities and Research (MIUR) through the Aegis of the "Fondo per il finanziamento dei dipartimenti universitari di eccellenza" Initiative by the Project Internet of Things: Sviluppi Metodologici, Tecnologici E Applicativi under Grant Law 232/2016 (2018–2022). *(Corresponding author: Michele Zenari.)*

Michele Zenari, Matteo Buffolo, Mirko Fornasier, Carlo De Santi, Gaudenzio Meneghesso, and Enrico Zanoni are with the Department of Information Engineering, University of Padua, 35131 Padua, Italy (e-mail: michele.zenari@dei.unipd.it; matteo.buffolo.1@unipd.it; mirko.fornasier@unipd.it; carlo.desanti@unipd.it; gauss@dei.unipd.it; zanoni@dei.unipd.it).

Jeroen Goyvaerts, Sulakshna Kumari, Roel Baets, and Günther Roelkens are with the Photonics Research Group, IMEC, Ghent University, 9052 Gent, Belgium (e-mail: jeroen.goyvaerts@ugent.be; sulakshna09@gmail.com; roel.baets@UGent.be; gunther.roelkens@UGent.be).

Alexander Grabowski, Johan Gustavsson, and Anders Larsson are with the Photonics Laboratory, Department of Microtechnology and Nanoscience, Chalmers University of Technology, 412 96 Göteborg, Sweden (e-mail: alexander.grabowski@chalmers.se; johan.gustavsson@chalmers.se; anders.larsson@chalmers.se).

Andim Stassren is with IMEC, 3001 Leuven, Belgium (e-mail: andim.stassen@imec.be).

Matteo Meneghini is with the Department of Information Engineering, and the Department of Physics and Astronomy, University of Padua, 35131 Padua, Italy (e-mail: matteo.meneghini@unipd.it).

Color versions of one or more figures in this article are available at https://doi.org/10.1109/JQE.2023.3283514.

Digital Object Identifier 10.1109/JQE.2023.3283514

[10] can be achieved. The concept behind this method consists in growing the VCSEL on its native substrate (i.e. GaAs); then, after appropriate on-wafer testing, the device is detached from the substrate by means of a sacrificial layer incorporated in the layer stack, which is selectively etched after device fabrication. The detached III-V device is finally transferred to the silicon platform, on top of suitable coupling structures, using a stamp. The typical coupling structure is composed of a diffraction grating that couples the output optical mode of the laser to a waveguide that re-directs the light into the PIC [11]. Through this technique, VCSELs can be integrated with SiN waveguide circuits, forming so-called Vertical-Cavity Silicon-Integrated Lasers (VCSILs), which are the devices studied in this paper.

In the last 30 years the most common failure modes, causes, and mechanisms observed in oxide VCSELs have been addressed from different perspectives. One of the major sources of VCSEL failures is related to the oxide aperture. Indeed, after AlGaAs or AlAs oxidation, a significant stress is induced in the proximity of the oxide layers, causing the generation of cracks and/or dark line defects (DLDs) [12]. Concerning the external factors that lead to VCSEL failure, the diameter of the oxide aperture (typically ranging from a few microns up to about 10 microns) makes these devices sensitive to electrostatic discharge (ESD) and electrical overstress (EOS) [13]. Other common factors that cause the acceleration of VCSEL aging are thermally-induced degradation and current-driven defect generation [14] which are responsible for generating and propagating defects in the device. Also humidity was proven to produce different failure modes, including dislocation growth, semiconductor cracks, and optical window surface degradation [15]. Even though the degradation and failure of VCSELs have been widely studied in the past [16], [17], in the literature, only few papers dealt with the novel VCSILs, and the related reliability has never been addressed.

To analyze the degradation of these novel family of devices we carried out a series of constant-current stress tests, during which the devices are biased at constant current, and the kinetics of degradation are measured as a function of time. We repeated the same test for four different current levels (2.5, 3.5, 4.0, and 4.5 mA) at the same ambient temperature (25°C) for observing the degradation kinetics versus current. As an outcome of this first-time-analysis, we identified two phases of degradation, labeled Phase 1 (Ph1) and Phase 2 (Ph2) respectively. Remarkably, during Ph1, a worsening of the threshold current was observed, whereas Ph2 also highlighted the degradation of the subthreshold slope. The peculiar degradation kinetics allowed us to correlate the worsening of the optical characteristics to the diffusion of impurities through the top DBR (Distributed Bragg Reflector) (Ph1) first, and in the active region of the laser during Ph2.

II. Samples Under Investigation

The devices analyzed within this work are vertical-cavity silicon-integrated lasers emitting at 845 nm. Each device consists of a III-V VCSEL, designed for bottom-emission, and a SiNx waveguide realized on a silicon substrate. The structure, starting from the top, includes a Ti/Pt/Au disk-shaped p-contact that serves both as electrode and as a top reflector. The top DBR is p-doped with carbon and consists of 29 mirror pairs of $Al_{0.12}Ga_{0.88}$ As/$Al_{0.90}Ga_{0.10}$ As. At the bottom of the p-DBR, within the layer closest to the separate confinement heterostructure (SCH) region, a 30 nm $Al_{0.98}Ga_{0.02}As$-layer is included for the formation, through selective wet oxidation, of an oxide aperture about 4 μm wide. The presence of this aperture laterally confines both the current and the optical mode to the center of the circular VCSEL structure. The active area of the laser is located below the aperture and consists of a $1 - \lambda$ thick SCH and a multi-quantum-well (MQW) structure containing five 4 nm thick $In_{0.10}Ga_{0.90}As/Al_{0.37}Ga_{0.63}As$ QWs. The bottom DBR is n-doped and is composed of 23 mirror pairs of $Al_{0.12}Ga_{0.88}As/Al_{0.90}Ga_{0.10}As$. A Ni/Ge/Au n-contact is positioned a few DBR mirror pair layers below the active area. At the bottom of the n-DBR, a 527 nm $Al_{0.12}Ga_{0.88}As$ buffer layer is included to tune the cavity length between the bottom DBR and the diffraction grating. Underneath this layer, a 4 nm GaAs layer serves as an etch stop layer with respect to an $In_{0.49}Ga_{0.51}P$ sacrificial layer, which is required for the micro-transfer-printing process, as will be discussed below. The thin GaAs layer absorbs light at 850 nm, although the impact is minimized since the etch stop layer is placed outside of the III-V cavity and the standing wave pattern has a node at the thin GaAs layer.

Below the VCSEL, aligned with the oxide aperture, a diffraction grating was placed to couple the optical mode into a SiN/SiO_2 waveguide. The grating also provides polarization-dependent and mode-selective feedback, resulting in an extended cavity laser defined by the top oxide thickness of the cladding above the waveguide (WG). The polarization selective feedback lowers the TE threshold gain to a value smaller than the TM threshold gain. As a result, the VCSIL preferentially lases in TE-polarization and out-couples the light laterally into two SiN_x waveguides to form the vertical-cavity silicon-nitride-integrated laser structure. The light inside the waveguides propagates in both directions, and is out-coupled by means of a grating coupler [18] located on each side. Fig. 1 depicts a simplified schematic of the devices under test. Further information regarding the device epitaxy, growth and fabrication can be found in [19].

III. Methodology

For our experimental purposes, the samples have been aged and characterized on-wafer. Temperature control was achieved through a TEC-controlled baseplate. The electrical characterization was performed by means of an HP 4142 source-meter. The L-I measurements were carried out through a Thorlabs S120VC amplified Si photodiode. To perform electroluminescence (EL) spectral measurements, we employed an Instrument System CAS140 spectrometer coupled to an optical fiber placed on top of one of the two output grating couplers of the chip. The impedance measurements were performed by means of a Keysight E4980A LCR meter. Both stressing and characterization were carried out at a fixed baseplate temperature of $T_{AMB} = 25$ °C.

To evaluate the degradation kinetics as a function of time, the devices were submitted to a constant-current stress

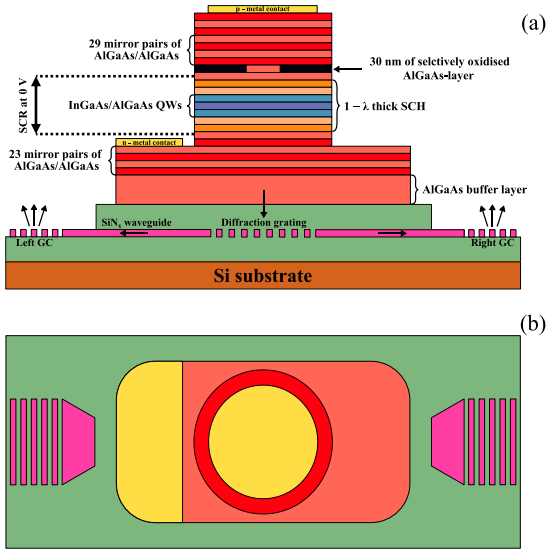

Fig. 1. Simplified view of the samples under investigation. a) cross-section schematic and b) top view. The drawing is not scaled according to the actual geometry of the device.

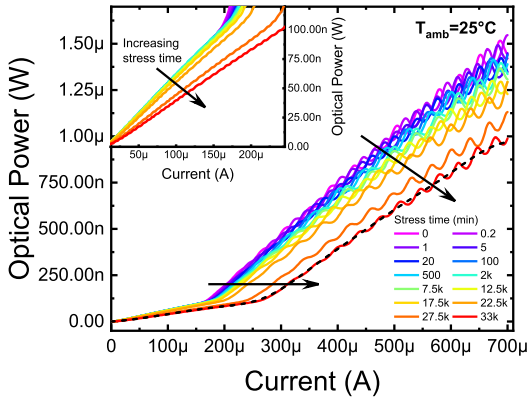

Fig. 2. Variation of the L-I curves during stress (I_{stress} =3.5 mA). The inset highlights the degradation of the OP_{sub} slope, which does not correlate with the variation of I_{th} during the initial phases of stress. The dashed black line represents the post-stress curve with applied digital LP filter.

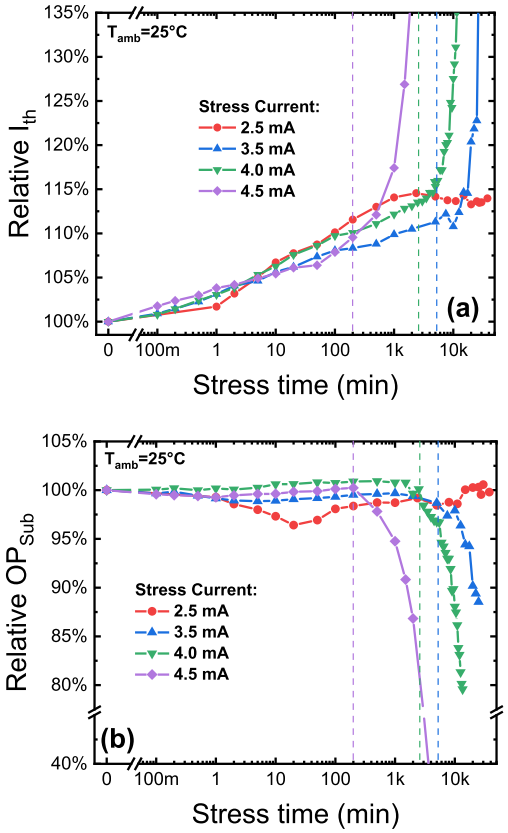

Fig. 3. a) I_{th} degradation kinetics as a function of stress time for different I_{stress}. b) OP_{sub} degradation kinetics as a function of stress time for different I_{stress}. By comparing the two figures, the reader can identify the activation of Ph2 by looking at the onset of Sub_{th} degradation (also highlighted by vertical dashed lines).

experiment. The stress experiment was interrupted at different stages to evaluate the effects of device degradation by carrying out both electrical (I-V, C-V, and C-f) and optical (L-I and spectra) measurements. In this work, we analyze the results of four constant current aging tests carried out at stress levels ranging from 2.5 mA to 4.5 mA. Considering that the diameter of the oxide aperture is 4 μm wide, and the average threshold current at RT is about 170 μA ($\approx$ 1350 A/cm^2), the corresponding stress current density lies within the 19.9 - 35.8 kA/cm^2 window, thus representing a highly accelerated stress condition.

IV. Constant Current Stress Results

A. Optical Degradation Modes

To analyze the optical degradation modes that were found to affect the samples under investigation, we start by reporting the detailed stress-induced variation of the L-I curves during aging at I_{stress} = 3.5 mA, chosen as a representative stress scenario (Fig. 2). The L-I characteristics show a superimposed sinusoidal "ripple": this behavior derives from the optical feedback associated with the extended optical cavity formed by the SiN waveguide and the grating coupler. To correctly extrapolate typical device parameters, such as threshold current (I_{th}), slope efficiency (SE), and sub-threshold slope (OP_{sub}), the raw L-I data have been processed by means of a digital low pass filter, thus obtaining a more familiar piece-wise linear output characteristic.

Initially, the devices were found to only exhibit an I_{th} increase, as well as a minor decrease in SE, whereas the OP_{sub} starts to decrease only after a certain amount of time from the beginning of the stress (see the inset of Fig. 2). Considering this, we can recognize two distinct phases of degradation: a phase 1, labeled Ph1, during which only I_{th} is worsening, and a phase 2 (Ph2), during which both I_{th} and OP_{sub} are degrading. This behavior is peculiar, since the absence of correlation between the increase in I_{th} and the optical emission in subthreshold regime may indicate that the aging procedure is progressively affecting different parts of the III-V structure, as will be discussed in the following paragraphs.

B. Dependence of the Optical Degradation Modes on Stress Current

With the aim of further discriminating the stress phase-dependent degradation processes affecting the optical characteristics of the devices, the impact of stress current will now be discussed. Fig. 3a and Fig. 3b show, respectively, the

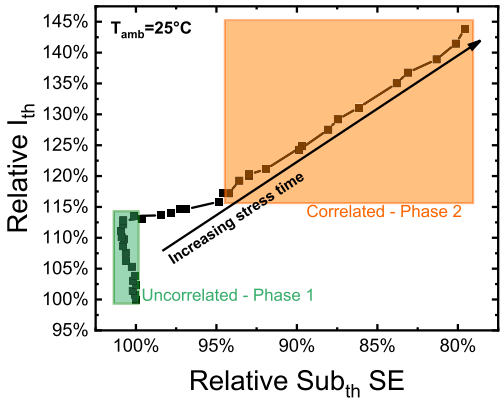

Fig. 4. Correlation between the threshold current increase and the sub-threshold slope decrease (I_{stress} =4.0 mA).

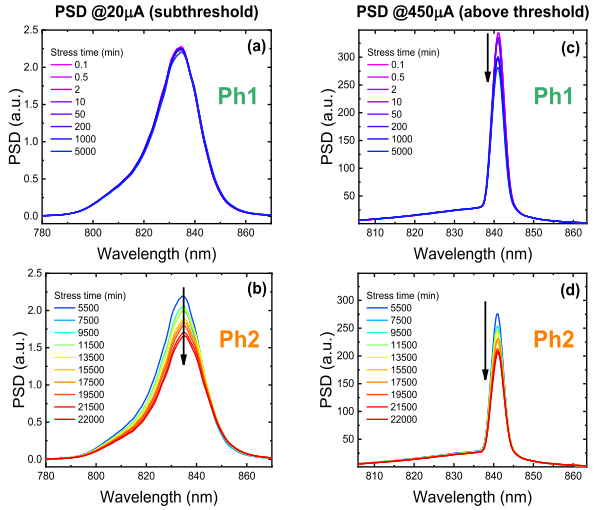

Fig. 5. Spectra collected during stress: a) spontaneous emission during Ph1, b) spontaneous emission during Ph2, c) laser emission during Ph1 d), laser emission during Ph2 (the reader should notice that the x-axes scales related to the plots on the left and on the right are different).

trends of I_{th} and Sub_{th} slope as a function of stress time, for I_{stress} = 2.5, 3.5, 4.0, and 4.5 mA.

From the experimental results reported above the following observations can be made:

- the degradation rate during Ph1 does not depend on the stress current level (within the stress current range explored), i.e., the threshold current degradation process does not seem to be strongly current-activated during the initial phase of degradation.
- Ph1 saturates as threshold current increases by 8-15 % with respect to its original value. This behavior can be easily seen by looking at the 2.5 mA stress test, during which Ph2 is not activated and the I_{th} increase saturates at ≈12 % after about 2000 min of stress.
- In correspondence to the onset of Ph2, the devices start exhibiting a lowering of OP_{sub}, correlated with a second threshold current increase process.
- The onset of activation of Ph2 strongly depends on the level of applied stress current and is accelerated as stress current is raised.

To better analyze the relation between the I_{th} and the OP_{sub} degradation, we compared their two trends to look for a possible correlation. Fig. 4 shows that during Ph1 I_{th} and OP_{sub} are not correlated. On the other hand, during Ph2 the two quantities are linearly correlated.

The correlation between I_{th} and OP_{sub}, which indicates the simultaneous worsening of both device parameters, has often been observed in the past [20], [21], and can typically be ascribed to the generation/migration of defects, acting as non-radiative recombination centers (NRRCs), in the active region of the laser. This kind of degradation mechanism increases the current required to reach lasing threshold and lowers the optical efficiency in subthreshold, i.e., LED-like, emission regime. Indeed, if we evaluate the below-threshold rate equation for a carrier density equal to its value at threshold (N_{th}), and if we assume that the injection efficiency, η_{inj}, below and above-threshold is the same, we can write that [22]:

$$\frac{\eta_i I_{th}}{qV} = \left(A + BN_{th} + CN_{th}^2\right) N_{th} = \frac{N_{th}}{\tau} \tag{1}$$

that yields:

$$I_{th} = \frac{qVN_{th}}{\eta_i \tau} = \frac{qV\left(A + BN_{th} + CN_{th}^2\right) N_{th}}{\eta_i} \tag{2}$$

Here A, B, and C are the Shockley-Read-Hall, the radiative and the Auger recombination coefficients, q is the electron charge, τ is the average carrier lifetime and V is the volume of the active region. Therefore, both the sub-threshold slope, given by [23],

$$OP_{sub} \propto \frac{N}{\tau} = N(A + BN + CN^2) \tag{3}$$

and the threshold current (Eq. 2), strongly depend on the balance between radiative (BN^2) and non-radiative ($AN + CN^3$) recombination terms. For this reason, assuming that the variation of the Auger coefficient (CN^3) due to the variation of N_{th} is lower than the increment of the SRH (Shockley-Read-Hall) term due to the A coefficient, the strong correlation observed between the trend of I_{th} and OP_{sub} suggests that their worsening during constant-current aging can be ascribed to the increase in SRH recombination rate, possibly due to the generation/relocation of impurities, that reach the active region in correspondence to the onset of Ph2.

C. Spectral Variations Induced During the Aging Procedure

To further prove our hypothesis on the physical origin of the degradation process occurring during Ph2, we repeated a constant current stress by recording also the EL spectra at two current levels: at 20 μA, to evaluate the spontaneous emission spectra below threshold, and at a current of 450 μA, to measure spectra above threshold, where optical emission mostly originates from stimulated recombination. The stress current in this case was set at 3.5 mA, since this stress level was found to be capable of triggering the onset of Ph2 in a reasonable amount of time (< 40000 min), as indicated by the previously reported stress experiments.

The experimental results reported in Fig. 5 reveal that the spontaneous emission is only affected during Ph2, whereas

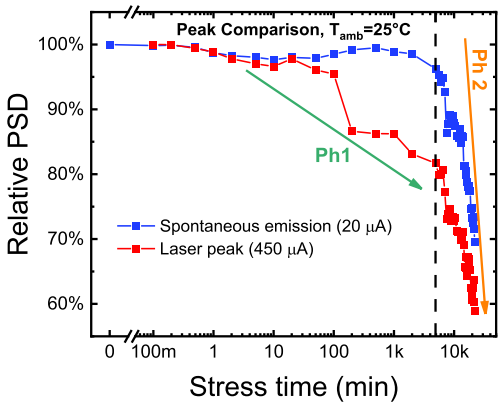

Fig. 6. Integrated PSD trends from Fig. 5: laser peak degradation vs spontaneous emission peak degradation (I_{stress} =3.5 mA).

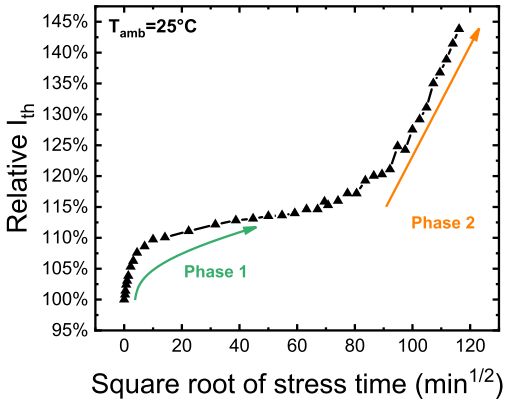

Fig. 7. I_{th} degradation as a function of the square root of stress time (I_{stress} =4.0 mA).

the stimulated emission degrades both during Ph1 and Ph2. The integrated power spectral density (PSD) trends, reported in Fig. 6, show the different behavior of the two components during stress: the laser emission features a relative decrease of about -17% during Ph1, whereas the spontaneous emission is unaltered, confirming the outcome of the L-I measurements. Since during Ph1 only the stimulated emission exhibits relevant worsening, it is unlikely that degradation is taking place within the active region, since in this case also the spontaneous emission would be influenced. In other words, if defects would reach the active region causing an increment of the SRH recombination (increment of A coefficient), according to Eq. 2 and 3 this would imply both the lowering of OP_{sub} and the increment of I_{th}. For this reason, we suppose that Ph1-related optical degradation is probably due to the worsening of the DBR reflectivity, or to an increase in optical absorption, according to [23]:

$$\alpha_{tot} = \alpha_i + \frac{1}{2L} ln\left(\frac{1}{R_1 R_2}\right) \tag{4}$$

where α_{tot} is the total absorption coefficient, α_i represents the internal losses, L is the cavity length and $R_{1,2}$ is the mirror reflectivity. Indeed, unlike the spontaneous emission which is uncoupled with modes of the cavity, the value of the threshold current strongly depends on the optical feedback provided by the DBRs. Based on this consideration, we propose that during Ph1 the optical degradation is mainly caused by the generation/relocation of impurities that create optically-active deep levels responsible for increasing the optical losses within the cavity, thus worsening the stimulated emission [24].

D. Analysis of the Degradation Kinetics

To better understand the degradation dynamics determining the observed threshold current increase, we further analyzed the time-dependence of the degradation process. The plot of the trend of I_{th} as a function of the square root of stress time [25], reported in Fig. 7, indicates that the degradation curve has a square-root dependence on stress time, during Ph2.

This kind of temporal dependence suggests that degradation during Ph2 may be proceeding through the diffusion of impurities acting as non-radiative recombination centers toward the active region of the devices [25]. When impurities diffuse from a region where their concentration N_0 is constant, the temporal variation in concentration $N(z, t)$ at a given depth z follows Fick's laws of diffusion and can be expressed by:

$$N(t, z) = \frac{N_0}{\sqrt{4\pi Dt}} e^{-\frac{z^2}{4Dt}} \tag{5}$$

where D is the diffusion coefficient of the moving impurity. Since the density of the diffusing NNRCs directly impacts on the non-radiative lifetime τ_{nr} (assumed to be dominated by the SRH recombination rate), also the decrease in the non-radiative lifetime is supposed to have a square-root dependence on time.

In addition to that, we can also notice that between Ph1 and Ph2 there is an intermediate phase during which I_{th} experiences a very limited degradation ($\approx$ +2.5%), while maintaining a weaker dependence on the square root of stress time compared to Ph2: as a matter of fact, the slope of the plot from 2500 min to 6500 min is lower, possibly indicating a variation of the apparent diffusion coefficient. Generally speaking, this kind of variation can either be indicative of i) a change in the diffusing species or ii) a change in the diffusing environment. Concerning the latter hypothesis, this could indicate that during Ph2 the impurities are diffusing through a different region, like the device layers closer to the active region, where their presence impacts in a different way on the radiative efficiency of the device. These considerations further support the hypothesis on the relocation of NRRCs toward the active region occurring during Ph2.

E. Analysis of the Stress-Induced Variation in the Series Resistance During Stress

Additional evidence of the stress-induced diffusion of impurities is provided by the variation of the differential series resistance (R_S) calculated from the I-V characteristics collected during stress. By comparing the I_{th} and the R_S kinetics (Fig. 8), we can observe that the series resistance rapidly increases during the early stages of Ph1 and saturates after the first 5-10 minutes of stress. Considering the structure of the device, the series resistance is mostly determined by the oxide aperture, and the current spread within the top

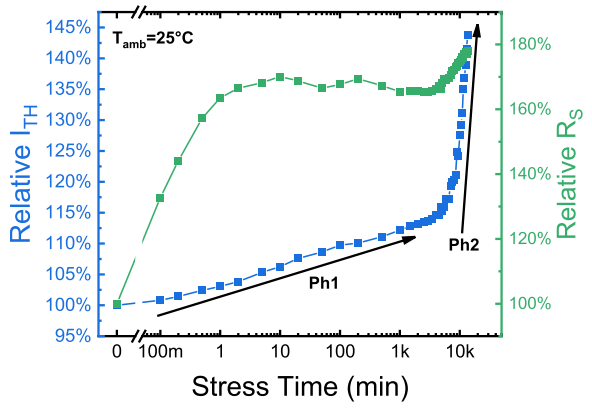

Fig. 8. Threshold current (I_{th}) and series resistance (R_S) vs stress time (I_{stress} =4.0 mA).

DBR [26]. The observed variation in R_S can therefore be ascribed to the relocation of impurities that passivate the p-type dopant (carbon in our devices) and/or that create complexes that increase the intrinsic series resistance of the DBR, due to the local accumulation of fixed charge. In particular, the large series resistance variation may be probably originated by the passivation of the dopant species in the device structure. Indeed, the variation of the doping profiles can induce the generation of anomalous potential barriers in both conduction and valence bands capable of causing such series resistance increment. Such anomalous series resistance variation may be originated from the suboptimal p-contact process described in the previous paragraphs. For instance, hydrogen was proven to form complexes with carbon atoms used as a p-type dopant in GaAs. In particular, the interaction between hydrogen and carbon can lead to the formation of H-C_{As} and H-C_{Ga} complexes, that induce the passivation of the doping properties of C in many III-V semiconductors [27]. This interpretation supports the hypothesis on the generation of optically-active deep levels that can absorb coherent photons and favor the increase in the p-DBR losses previously described.

Figure 8 also reveals that after the first series resistance increase, a second variation, smaller than the first one, starts occurring in correspondence of the activation of Ph2. Since in this case the electrical degradation is found to be correlated with the I_{th} increase, this may indicate that when the impurities approach the active region they originate a second R_S increment, possibly due to their interaction with the narrow and thin semiconductor layers associated with the oxide-confined aperture.

V. Capacitance Spectroscopy Analysis

To better pinpoint the device regions affected by the relocation of defects, as well as their specific role in the degradation of the VCSILs, we analyzed the variation of the small signal impedance of the device induced by the constant current stress by means of capacitance-voltage (C-V) and capacitance-frequency (C-f) measurements. Fig. 9a reports the capacitance-voltage curve (C-V) before and after the stress: from these plots we can notice that the stress test induced a capacitance increment only at forward bias voltages (> 0.5 V),

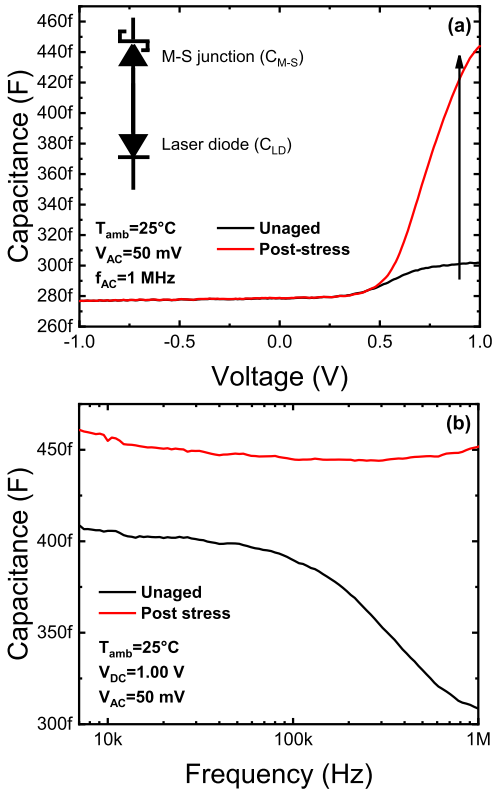

Fig. 9. a) C-V curves of a VCSIL measured at 1 MHz before and after stress. The picture in the graph shows the proposed equivalent electrical model of the device. b) variation of the C-f curves measured at 1 V after stress at I_{stress} = 3.5 mA. Measurements data below 7 kHz were not shown due to the measurement noise.

whereas minimal variations affected the C-V characteristics at more negative bias levels. To investigate the physical origin of this variation, the C-f profiles have also been measured for bias levels between 0 V and 1 V to study the cause of the capacitance variation in the C-V profile. Fig. 9b depicts the C-f profile measured in the latter DC bias conditions: remarkably, the data indicate i) the presence of a capacitance decrease for frequencies above 100 kHz, and ii) that this variation can no longer be detected on the aged device. The behavior observed for the fresh device can be associated with the response of a defect located at the edge of the SCR (space charge region) being filled and emptied as a consequence of the variation of the small-signal voltage (V_{AC}) [28], [29]. We analyzed the derivative of capacitance with respect to frequency versus angular frequency ($dC/df vs\ \omega$) over a reasonable temperature range, to track the shift of the peak associated with the defect response (Fig. 10a). This technique, known as Thermal Admittance Spectroscopy (TAS) [28], allows to relate the small signal capacitance inflection point with the thermal emission rate of the trap through the following relation:

$$e\,(T) = \frac{\omega_i}{0.825} \tag{6}$$

where $e\,(T)$ is the thermal emission rate at a given temperature T and ω_i is the angular frequency at the inflection point. The activation energy of the trap (E_a) can then be obtained by measuring the small signal capacitance inflection point at

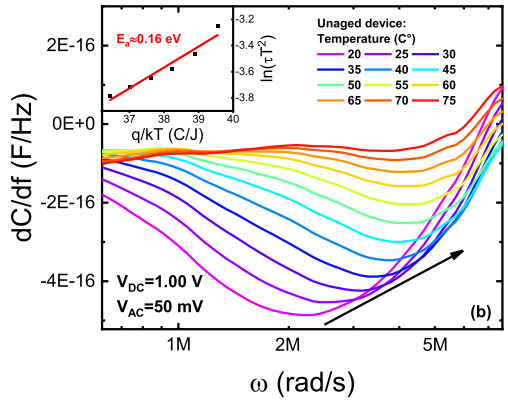

Fig. 10. Variation of the derivative of capacitance with respect to frequency versus angular frequency (dC/df vs ω) over temperature; the peak of the capacitance derivative corresponds to the inflection point of the capacitance curve; the slope of Arrhenius plot in the inset graph yields an activation energy for the defect responding to the AC stimulus of Ea $\approx$ 0.16 eV.

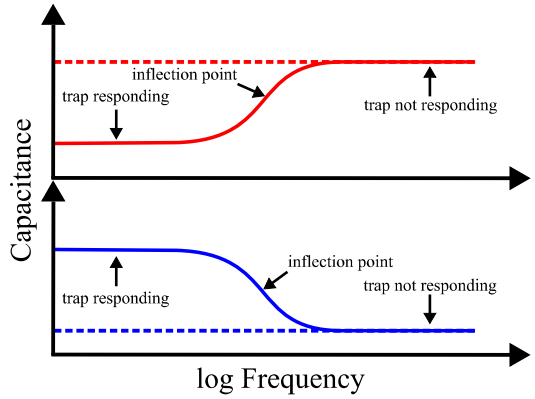

Fig. 11. Study of capacitance-frequency profiles: the blue line represents the behavior of a majority carrier trap whereas the red curve the response of a minority carrier trap. The dashed lines depict a non-responding defect in both cases.

different temperatures and by building the related Arrhenius plot, from the mathematical relation expressed by Eq. 7.

The experimental data were used to build the Arrhenius plot shown in the inset of Fig. 10. The resulting E_a, about 0.16 eV, indicates the presence of a shallow defect, located close to one of the two band edges. Looking at the response of the C-f curve we can assess the type of defect involved. From the sketch reported in Fig. 11, we can see that at low frequencies, when the trap follows the small signal modulation, the measured value of the small signal capacitance (or equivalently of the conductance) becomes affected by the presence of the defect. On the other hand, at high measuring frequencies, the modulating signal is much faster than the emission/capture rate of the trap, and therefore the small signal capacitance falls back to its expected theoretical value Fig. 11. To be more specific, when dealing with a majority carrier trap the value of the capacitance is lower at higher frequencies, since in this case the trap state cannot be emptied quickly enough and the filled defect exhibits a polarity which is opposite with respect to the fixed charge related to the ionized dopant atoms: this lowers the local charge density, thus inducing the widening of the space charge region and the lowering of the small signal capacitance, according to the relation given by

$$C = A \cdot \frac{\epsilon}{x_D} \tag{7}$$

where A is the junction area, ε is the material permittivity and x_D represents the extension of the space-charge region.

Conversely, when measuring the response of a minority carrier trap, the capacitance-frequency response shows an opposite variation due to the different polarity of defects. The minority carrier behavior is rarely observed when studying admittance vs frequency (Y-f) characteristics and SCR extension in semiconductor devices since the Fermi level is typically positioned far from the (minority carrier) trap energy level.

Based on these experimental observations, we developed two hypotheses that could explain the behavior and the variation of the capacitance measurements of the DUTs during stress:

1) A first interpretation relates the capacitance increment measured at positive bias levels during stress to the relocation of defects inside the active region. The presence of such defects increases the density of fixed charge, thus inducing the shrinking of the space charge region (x_D) and the increase in the measured small signal capacitance. This hypothesis is partially supported by the C-f variation during stress. Since we detect the response of the defect in the unaged device but not after the stress, the experimental data suggest that the defect moved from the edge of the space charge region (being modulated by the ac voltage) to another site. Moreover, the post stress C-f curve does not lay on the high frequency value of the unaged curve, as depicted in Fig. 11 (dashed blue line). This means that the trap is not responding anymore, because it has moved inside the SCR closer to the QWs implying a capacitance increment that explains the capacitance shift of the C-f curve.
2) A second interpretation relates the observed capacitance increment in the 0.5-1 V range (at 1 MHz) to the annealing of the p-contact, induced by the early phases of stress. In this case we assume that in the fresh device the metal-semiconductor (M-S) junction at the p-side exhibits a weak Schottky behavior, rather than acting as ohmic tunnel junction. As a consequence, the electrical model of the AC impedance of the device must also consider the presence of the depletion capacitance associated to the p-contact (referred to as $C_{M?S}$), which is connected back-to-back to the main laser diode capacitance (C_{LD}), as depicted in Fig. 11. To evaluate the total capacitance (C_{tot}) of the device we must then consider that:

$$C_{tot} = \frac{C_{LD} \cdot C_{M-S}}{C_{LD} + C_{M-S}} \tag{8}$$

When a reverse bias is applied to the VCSIL, the M-S junction is forward biased, so in series with the laser diode there is a very high capacitance and the lower depletion capacitance of the laser dominates the series of the two components. On the contrary, when the VCSIL is under forward bias, the M-S junction is reversely biased. If the contact is of Schottky-type, its depletion capacitance limits

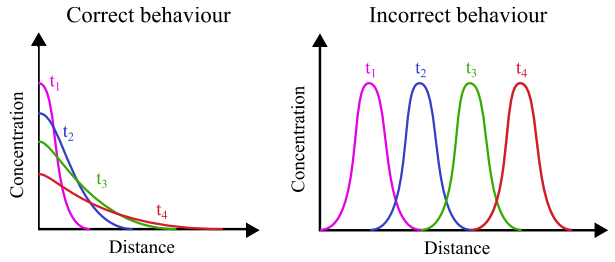

Fig. 12. Representation of a generic diffusion process: on the left the typical behavior is reported, whereas on the right we shown the incorrect kinetics that could be deduced from the first hypothesis proposed.

the overall AC capacitance of the device. After the contact annealing, which we assume to be occurring during the first part of Ph1, the contact becomes Ohmic (through tunneling). In this case the resulting capacitance is dominated by the laser capacitance in both bias regimes ($C_{tot} = C_{LD}$). Therefore, the variation of the C-f response can be explained by considering that: a) on the fresh device we can detect the defect from the C-f response, originating from the depleted region of the M-S junction (meaning that the defect is located in the top part of the p-DBR); b) after the contact annealing we can no longer measure the trap response, because we are only probing defects located at the edge of the laser diode SCR. Moreover, the probed defect may be the same one that, according to our hypotheses, starts diffusing from the top DBR (probed by the M-S junction modulation) during the worsening of the mirror properties and then reaches the active region, causing the onset of Ph2, that shows the degradation of the radiative emission.

Among these two hypotheses, we are more prone to consider the second to be the more realistic for the following reasons:

1) Considering the first scenario, it is not likely that the defect completely vanishes from one location to settle in another, since the diffusion of impurities rarely proceeds through a rigid shift of the impurity profile. As depicted in Fig. 12, the theoretical kinetics for a diffusion process implies a lowering of the peak together with the progress of the diffusion front, for this reason we would expect to measure a lowering in the defect response due to the lowering of the trap concentration rather than its complete absence after stress.
2) If we consider that defects reached the active region causing the increment of the capacitance, this would involve a capacitance increment not only in forward but also in reverse bias regime (instead we only see an increment in the 0.5 - 1 V range).
3) Taking into account the previous consideration, a capacitance increment of ≈142 fF at 1 V (from 302 to 444 fF) should originate from a reduction in the space charge region width of ≈44%. This kind of variation would not be plausible in our case, as both the n and p sides of the laser are heavily doped ($>1{\cdot}10^{18}$ cm^{-3}), therefore modification should be induced by the migration of a very large amount of charged impurities towards the junction or the intrinsic region.
4) Finally, the capacitance shift observed by comparing the C-f profile before and after the stress (at 1 V) is compatible with the capacitance increment measured at 1 V in the C-V measurement (1 MHz). This points out why the plateau of the post stress curve did not lay on the high frequency value of the unaged C-f curve as expected from the theory when measuring a non-responding trap (Fig. 11). Indeed, this further proves that we are not measuring the trap because we are not probing within the SCR of the M-S junction that disappears with the annealing due to the stress, which, in turn, is responsible of the capacitance increment in both C-f and C-V characteristics.

VI. Modeling of the Optical Degradation Process

The outcome of the analysis presented so far can be summed up as follows:

- The stress procedure induces two distinct degradation processes, which are activated in two different time frames, referred to as Ph1 and Ph2, respectively. During the former, only the threshold current of the laser exhibits degradation, whereas during Ph2 the device exhibits the worsening of both I_{th} and OP_{sub}.
- Concerning Ph1, we related the degradation of I_{th} to the worsening of the mirror performance explaining the unaffected OP_{sub} over this first phase of degradation.
- From the interpretation of the capacitive measurements, we found out that in the unaged device a defect was possibly located closer to the p-contact (in the top part of the DBR), whose signature was not detected after the stress. This defect could be responsible for the increased losses in the top DBR that during Ph1 affected only the I_{th}. The defect is probably measured within the SCR of the parasitic M-S junction. Indeed, the SCR of the laser diode cannot extend much further than the intrinsic region due to the heavily doped DBRs. According to our simulations the SCR is 312 nm at -3 V whereas at +1 V is 303 nm, therefore it does not extend far beyond the intrinsic region (283 nm). For a qualitative view of the extension of the SCR in the device structure at 0 V see Fig. 1.
- During Ph2 we observed a linear correlation between OP_{sub} and I_{th}; the relation among these two quantities was also confirmed by analyzing the spontaneous and the stimulated emission from the spectra. These outcomes suggested that over the last phase of degradation, defects acting as NNRCs reached the active region, thus worsening the radiative recombination.
- Also, this last point is again compatible with the study of the C-f profiles, as the same defect probed in the fresh device can move through the top DBR in the Ph1 and finally reach the active region determining the beginning of Ph2.

According to the experimental results provided within this work, the devices show a very unusual degradation process never found in common VCSELs. Indeed, the proposed two-phase degradation model takes into account the migration of point defects during the stress, rather than the generation/propagation of extended defects after the device growth [16]. Remarkably, we managed to correlate the variation of the laser characteristics with the regions crossed by impurities

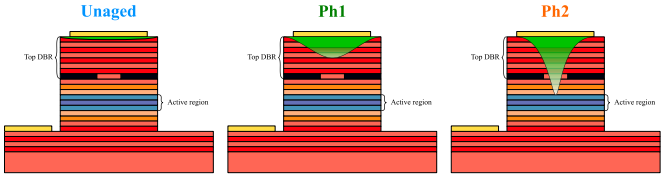

Fig. 13. Schematic illustration of the proposed degradation model: during Ph1 impurities are crossing the top DBR, whereas over Ph2 impurities reach the active region.

a specific aging time. Furthermore, the first degradation phase (Ph1), related to the worsening of the top DBR properties of a VCSEL, was never reported in the literature. Indeed, the only report analyzing the degradation of reflection induced by thermal annealing in a GaAs-based DBR can be found in [31], which should be the case, since the driving force required to induce the alloy disordering described in [31] would not be present, or strong enough, during the aging procedure adopted in this case of study. According to the results of our study, the impurities are coming from the p-contact layers, therefore, we do not exclude that degradation is originated from the possible non-optimal p-contact growth and/or processing.

VII. Conclusion

In summary, with this work, we have analyzed for the first time the physical degradation processes related to vertical-cavity silicon-nitride-integrated lasers, emitting at 845 nm, for silicon photonics applications. We studied these devices by carrying out several constant current stress tests in which we performed optical (L-I and spectra) and electrical (I-V, C-V, and C-f) measurements. The experimental results showed two different phases of degradation: during phase 1, only I_{th} was found to degrade whereas both I_{th} and OP_{sub} changed during phase 2. According to our analysis, this uncommon optical degradation was found to proceed through an impurity diffusion process: the diffusive front is supposed to start from the top p-DBR, and then reaching the active region (Fig. 13). Degradation was found to take place in two distinct phases: during Ph1 impurities move through the top DBR, causing the increase of the mirror losses and the observed increase in the sole threshold current. The amount of degradation and its rate during this phase do not depend on the stress current. The assumption that impurities are moving through the top DBR is supported by the increment of the series resistance that could be originated by the passivation of the p-type dopant or by the formation H-C_{As} and H-C_{Ga} complexes. Moreover, additional capacitance measurements also confirmed the presence of a defect in the unaged device, possibly located closer to the anode, which is no longer observed after the first stages of stress. We suppose that in the fresh device impurities are passivating the anode contact, forming a Schottky-type junction; after an initial contact annealing, these impurities migrate away allowing the formation of a tunnel junction at the p-contact. During Ph2 the impurities finally reach the active region where they act as NRRCs, inducing the degradation of both threshold current and sub-threshold slope. The outcome of this analysis suggests that the lifetime of current state-of-the-art VCSILs may be further increased by improving the processing/growth of the p-type contact layers of the device. The result of the study suggests that the same strategy to improve the devices lifetime can be valid for generic laser diodes based on similar III-As epitaxies. Indeed, the processing and growth of contact layers can be critical not only for the devices analyzed within this work, but also for other types of lasers, edge emitting as well, featuring different type of integration strategies (heterogenous, hybrid or fully epitaxial).

References

[1] N. Margalit, C. Xiang, S. M. Bowers, A. Bjorlin, R. Blum, and J. E. Bowers, "Perspective on the future of silicon photonics and electronics," *Appl. Phys. Lett.*, vol. 118, no. 22, May 2021, Art. no. 220501.

[2] Z. Fang and C. Z. Zhao, "Recent progress in silicon photonics: A review," *ISRN Opt.*, vol. 2012, pp. 1–27, Mar. 2012.

[3] R. Chandrasekar, Z. J. Lapin, A. S. Nichols, R. M. Braun, and A. W. Fountain, "Photonic integrated circuits for department of defense-relevant chemical and biological sensing applications: State-of-the-art and future outlooks," *Opt. Eng.*, vol. 58, no. 2, p. 1, Feb. 2019, doi: 10.1117/1.OE.58.2.020901.

[4] J. M. Morales, P. Cho, J. R. Bickford, P. M. Pellegrino, G. Leake, and M. L. Fanto, "Development of army relevant wearable Photonic Integrated Circuit (PIC) biosensors," *Proc. SPIE*, vol. 11749, pp. 98–106, Jan. 2021, doi: 10.1117/12.2587098.

[5] C. Cheng, W. Lo, B. Su, C. Wu, and G. Lin, "Review of VCSELs for complex data-format transmission beyond 100-Gbit/s," *IEEE Photon. J.*, vol. 13, no. 5, pp. 1–13, Oct. 2021.

[6] N. N. Ledentsov et al., "High speed VCSEL technology and applications," *J. Lightw. Technol.*, vol. 40, no. 6, pp. 1749–1763, Mar. 15, 2022.

[7] D. Gerthsen, F. A. Ponce, G. B. Anderson, and H. F. Chung, "Lattice mismatch effects in GaAs epitaxy on Si and GaP," *MRS Proc.*, vol. 122, pp. 21–26, Jan. 1988.

[8] P. Kaur, A. Boes, G. Ren, T. G. Nguyen, G. Roelkens, and A. Mitchell, "Hybrid and heterogeneous photonic integration," *APL Photon.*, vol. 6, no. 6, Jun. 2021, Art. no. 061102.

[9] A. Y. Liu, R. W. Herrick, O. Ueda, P. M. Petroff, A. C. Gossard, and J. E. Bowers, "Reliability of InAs/GaAs quantum dot lasers epitaxially grown on silicon," *IEEE J. Sel. Topics Quantum Electron.*, vol. 21, no. 6, pp. 690–697, Nov. 2015, doi: 10.1109/JSTQE.2015.2418226.

[10] K.-J. Boller et al., "Hybrid integrated semiconductor lasers with silicon nitride feedback circuits," *Photonics*, vol. 7, no. 1, p. 4, Dec. 2019, doi: 10.3390/PHOTONICS7010004.

[11] A. Rahim et al., "Open-access silicon photonics platforms in Europe," *IEEE J. Sel. Topics Quantum Electron.*, vol. 25, no. 5, pp. 1–18, Sep. 2019.

[12] R. W. Herrick, A. Dafinca, P. Farthouat, A. A. Grillo, S. J. McMahon, and A. R. Weidberg, "Corrosion-based failure of oxide-aperture VCSELs," *IEEE J. Quantum Electron.*, vol. 49, no. 12, pp. 1045–1052, Dec. 2013.

[13] D. T. Mathes, J. Guenter, B. Hawkins, B. Hawthorne, and C. Johnson, "An atlas of ESD failure signatures in vertical cavity surface emitting lasers," in *Proc. Int. Symp. Test. Failure Anal.*, Oct. 2005, pp. 336–343.

[14] K. Maeda, M. Sato, A. Kubo, and S. Takeuchi, "Quantitative measurements of recombination enhanced dislocation glide in gallium arsenide," *J. Appl. Phys.*, vol. 54, no. 1, pp. 161–168, Jan. 1983.

[15] S. Xie et al., "Failure mode analysis of oxide VCSELs in high humidity and high temperature," *J. Lightw. Technol.*, vol. 21, no. 4, pp. 1013–1019, Apr. 2003.

[16] Z. Yu-Qi et al., "Common failure modes and mechanisms in oxide vertical cavity surface emitting lasers," *Chin. Opt.*, vol. 15, pp. 187–209, Jan. 2022.

[17] R. W. Herrick, "Design for reliability and common failure mechanisms in vertical cavity surface emitting lasers," *MRS Proc.*, vol. 1432, pp. 9–20, Jan. 2012.

[18] Z. Liu, G. Muliuk, J. Zhang, G. Roelkens, N. Le Thomas, and R. Baets, "Micro-transfer printed silicon nitride grating couplers for efficient on-chip light coupling," *Proc. SPIE*, vol. 12004, pp. 10–14, Jan. 2022, doi: 10.1117/12.2626309.

[19] J. Goyvaerts et al., "Enabling VCSEL-on-silicon nitride photonic integrated circuits with micro-transfer-printing," *Optica*, vol. 8, no. 12, p. 1573, Dec. 2021.

[20] M. Buffolo et al., "Investigation of current-driven degradation of 1.3 μm quantum-dot lasers epitaxially grown on silicon," *IEEE J. Sel. Topics Quantum Electron.*, vol. 26, no. 2, pp. 1–8, Mar. 2020.

[21] M. Buffolo et al., "Degradation mechanisms of heterogeneous III–V/silicon loop-mirror laser diodes for photonic integrated circuits," *Microelectron. Rel.*, vols. 88–90, pp. 855–858, Sep. 2018.

[22] P. M. Smowton and P. Blood, "The differential efficiency of quantum-well lasers," *IEEE J. Sel. Topics Quantum Electron.*, vol. 3, no. 2, pp. 491–498, Apr. 1997.

[23] A. L. Coldren, W. S. Corzine, and L. M. Mašanović, *Diode Lasers and Photonic Integrated Circuits*. Hoboken, NJ, USA: Wiley, 2012, pp. 45–90.

[24] Y. M. Cheng, R. W. Herrick, P. M. Petroff, M. K. Hibbs-Brenner, and R. A. Morgan, "Degradation mechanisms of vertical cavity surface emitting lasers," in *Proc. Int. Rel. Phys. Symp.*, 1996, pp. 211–213.

[25] K. Orita et al., "Analysis of diffusion-related gradual degradation of InGaN-based laser diodes," *IEEE J. Quantum Electron.*, vol. 48, no. 9, pp. 1169–1176, Sep. 2012.

[26] V. P. Kalosha, V. A. Shchukin, and N. N. Ledentsov, "Comprehensive self-consistent analysis of oxide-confined vertical-cavity surface-emitting lasers," *Proc. SPIE*, vol. 10938, pp. 85–95, Oct. 2019.

[27] A. Amore Bonapasta, "Hydrogen passivation of carbon-doped gallium arsenide," *Phys. Rev. B, Condens. Matter*, vol. 48, no. 12, pp. 8771–8779, Sep. 1993.

[28] J. Barbolla, S. Dueñas, and L. Bailón, "Admittance spectroscopy in junctions," *Solid-State Electron.*, vol. 35, no. 3, pp. 285–297, Mar. 1992.

[29] M. Buffolo et al., "Defects and reliability of GaN-based LEDs: Review and perspectives," *Phys. Status Solid, A*, vol. 219, no. 8, Apr. 2022, Art. no. 2100727.

[30] P. Blood and J. W. Orton, *Electrical Characterization of Semiconductors: Majority Carriers and Electron States*. New York, NY, USA: Academic, 1992, pp. 517–542.

[31] P. D. Floyd and J. L. Merz, "Effects of impurity-free and impurity-induced disordering on the optical properties of GaAs/(Al,Ga)As distributed Bragg reflectors," *J. Appl. Phys.*, vol. 76, no. 9, pp. 5524–5527, Nov. 1994, doi: 10.1063/1.357153.